Contents lists available at ScienceDirect

# Biomedical Signal Processing and Control

# Adaptive denoising of 3D volumetric MR images using local variance based estimator

Pabitra Das [a,*], Chandrajit Pal [b], Amlan Chakrabarti [a], Amit Acharyya [b], Saumyajit Basu [c]

[a] A.K.Chaoudhury School of Information Technology, University of Calcutta, Kolkata 700106, India
[b] Advanced Embedded System and IC Design Laboratory, Department of Electrical Engineering, Indian Institute of Technology Hyderabad, India
[c] Park Clinic, 4, Gorky Terrace, Circus Avenue, Kolkata 700017, India

## ABSTRACT

Preservation of the anatomical structures during denoising of medical images is a very significant and challenging operation. Corruption of magnetic resonance image (MRI) by Rician noise is inherent to the acquisition process, affecting diagnosis. In this study, we present a novel filtering methodology that removes Rician noise from MRI by estimating the local noise variance, which drives the diffusion process of the filter. In our methodology, the adaptation of statistical edge stopping function captivates the preservation condition of the anatomical structure of the MRI images. The results obtained on synthetic/simulated MRI datasets (3D) and real MRI datasets confirm the accuracy and robustness of the proposed methodology. Compared to the benchmark approaches like BM4D, LTA3D, RNOLMMSE, ROLMMSE, MNL-tSVD and PRINLM3D, the optimized way of choosing the edge stopping functions, the automatic adjustment of the filtering coefficients and variance based local noise estimation technique lead to a qualitative and quantitative robust estimation performance, in case of both simulated and real datasets.

## 1. Introduction

MRI images are generally corrupted with a random noise that is accumulated during the acquisition process. This random noise drastically reduces the quality of acquired image and limits the accuracy of quantitative measurements of the magnetic resonance image (MRI) data. Besides it also affects the effectiveness of automatic computer analysis such as classification, registration, and segmentation. Thereby, making noise reduction a crucial pre-processing step for MRI images for proper clinical and research investigations. Several literatures on denoising filters have been proposed over the past decades dedicated to restore the MR images [1].

For denoising MRI images, a very well-known filtering approach namely anisotropic diffusion filter is used [2]. Sijbers et al. [3] have shown the methodology to reduce the bias by incorporating the Rice distribution into the noise filtering procedure for MRI data. McGibney and Smith [4] introduced signal and noise level descriptions in terms of their root-mean-square values for denoising. Wavelet based filters also works well for denoising specific type

of MRI images like f-MRI and T2-weighted MRI [5]. Krissian et al. [6] modeled a flux based diffusion filter for computed tomography (CT) and MRI data. The edge preservation was further improved by introduction of non-local means (NLM) filter, which was first proposed by Buades et al. [7] in 2005. Further modification in filtering process has been performed by applying directed principle of curvature on the NLM filter [8]. This has been followed by formulation of an estimation based filtering known as linear minimum mean square error (LMMSE) proposed by Aja-Fernández et al. [9] for denoising Rician noise for MRI data. To mitigate the existing parameter initialization problem in [8], Manjón et al. [10] proposed the parametric NLM filter (PRINLM) where the number of initialization parameters has been reduced. Following this an optimized 3D blockwise NLM filtering was proposed by Coupé et al. [11], which highly depends on the initialization of parameters. Further, Krissian and Aja-Fernández [12] introduced standard deviation of noise in the mean square estimation to create a modified version of linear minimum mean square error estimation procedure mentioned in [9].

Manjón et al. [13] has modified the existing NLM filter into a three dimensional rotational invariant one. Bhujle et al. [14] additionally introduced Laplacian of Gaussian filter in conjunction with NLM for filtering MRI. Golshan et al. [15] introduced a method to denoise MRI data, which is capable of choosing the samples, not

* Corresponding author.
 *E-mail address:* pdakc_rs@caluniv.ac.in (P. Das).

only from a local neighborhood but also from a large portion of a given region of pixels. Fu et al. presented a novel noise reduction method for 3D MR images based on low-rank tensor approximation [16]. But these filtering processes could not preserve the global and local structure of the MRI image simultaneously. Hu and Jiliu Zhou [17] removed the parameter initialization problem of NLM filter by introducing random sampling non-local mean (SNLM) algorithm, an optimized version of the NL-means filter for MRI noise removal. Pal et al. [18] proposed a diffusion based filter in addition to control the diffusion coefficient parameter responsible for diffusion filtering of the MRI. Baselice et al. [19] proposed a Maximum posterior estimator, adaptation to Markov random fields, developed for handling complex MRI data. Bayesian mean square error (BMSE) of the LMMSE estimator for volumetric MRI data denoising proposed by Golshan and Hasanzadeh [20]. Further Sudeep et al. and Yaghoobi et al. came up with a modified LMMSE estimator for filtering 3D-MRI images [21,22]. Very recently Baselice et al. proposed statistical distances (Kolmogorov–Smirnov distance) based NLM filter for MRI image data [23]. Sparse representation in transform-domain based filtering has also become a popular approach for image denoising Dabov et al. [24]. These type of filtering is based on the working principle of shrinkage of the transform spectrum, and inverse 3-D transformation. Further Maggioni et al. [25] in 2013 developed a 4-D transform-domain filter for volumetric MRI data computation. Recently, higher-order singular value decomposition (HOSVD) became a very popular approach for MRI image denoising. Rajwade et al. [26], Zhang et al. [27] and Khaleel et al. [28] proposed a 3D tensor-SVD for filtering MRI.

Kong et al. introduced a 4-D nonlocal transform-domain which is a modified nonlocal tensor-singular value decomposition technique, for denoising 3D MRI data [29].

Various popular techniques for filtering Diffusion Tensor MRI do exists. Lam et al. [30] reduced the Rician noise from DT-MRI data using Rank and Edge Constraints.

Recently Xia et al. [31] proposed a new denoising algorithm based on low-rank matrix approximation (LRMA) with regularization of weighted nuclear norm minimization (WNNM) to remove Rician noise of MR images. Though the NLM-based 3D MRI [32] filters can preserve edges better but it involves more computation time and includes an extra optimization variable as initialization parameter. The overall procedure can be interpreted as a progressive approximation in which the Rician noise denoising filter directs the remarkable search towards the solution.

The major challenges faced in the gradual improvement of MRI filtering in the past three decades are:

- Effectiveness of most of the denoising algorithms depend on error correction procedure present in signal to noise ratio (SNR) for noise estimation. This could not address the region based local noise variance.
- Requirement of additional parameters and its major dependence on the initialization of parameter.
- Its inefficiency in preserving the local and global anatomical structure.

To address the mentioned challenges we started investigating the local noise variance information for the estimation of the noise magnitude to be controlled by diffusion process through biweight estimator [33].

In this study, we propose a Rician noise removal filtering methodology, which takes into account the local noise statistical variance and controls the denoising through diffusion process. This local statistical variance information is utilized in the proposed biweight function (influenced by Tukey's) estimator, which additionally assists in preserving the edges as well as the fine texture information [34]. The proposed methodology is coined as *adap-*

*tive diffusion-based MRI filter* (ADMF3D). The implementation of the proposed ADMF3D is to provide an estimate of the Rician noise variance $Var(P)$ from the noisy data $I^t$. After noise estimation stage, ADMF3D is implemented in two stages, namely smoothing process and an adaptive diffusion-based filtering stage. The work-flow diagram as described above of our proposed methodology is illustrated in Fig. 1. The main highlights of our contribution are as follows:

- Tuning of diffusion coefficient, which controls the averaging process has been made adaptive, reducing its dependency on external additional parameters (explained in Section 3.1).
- Applied a statistical edge stopping function to preserve the details of anatomical structure of the MRI image both locally and globally (described in Section 3.2).
- We propose variance based local noise estimation methodology. Subsequently, extraction of local noise information influences the diffusion process leading to more efficient denoising (explained in Section 3.3).

We have also compared our methodology with some state-of-the-art techniques using synthetic and real (3D) MRI data respectively.

The paper is organized as follows. Section 2 describes the theoretical background and properties of Rician noise present in MRI image. Section 3 introduces the proposed local variance based estimator and adaptive diffusion-based MRI filter (ADMF3D). Experiments and results are discussed in Section 4. In this same section we have compared our result with other benchmark algorithms. Lastly, Section 5 conclude and discuss future scopes of the proposed methodology.

## 2. Theoretical background

A typical MRI image consists of a real and an imaginary part, which are reconstructed from the acquired data by the complex Fourier transform [35]. According to Henkelman [36] the uniform region of complex MRI image data $M$, in which the signal from the $j$th pixel, can be expressed as:

$$M_j = M_{Rj} + iM_{Ij} \tag{1}$$

where $(M_R)$ and $(M_I)$ are the real and imaginary parts respectively. The associated noise distribution in a MRI image follows the Rice probability distribution [37,38] and can be expressed with the probability density function as [36]:

$$f(P|m, \sigma_R) = \frac{P}{\sigma_R^2} \exp\left(\frac{-(P^2 + m^2)}{2\sigma_R^2}\right) I_0\left(\frac{Pm}{\sigma_R^2}\right) \tag{2}$$

where $\sigma_R$ is the Gaussian noise standard deviation in the complex domain of $M$, $P$ is the measured pixel intensity, $m$ denotes the magnitude of intensity, $m = \sqrt{M_R^2 + M_I^2}$ and $I_0$ represents the modified Bessel function with zeroth order of the first kind [39].

In case, if both the real and the imaginary parts have no signal, i.e. $m \to 0$, it indicates that the signal to noise ratio (SNR) is very small, i.e. $m/\sigma_R \to 0$. Thus, the Rice probability distribution becomes Rayleigh probability distribution, given by Eq. (3) [40]:

$$f(P, \sigma_R) = \frac{P}{\sigma_R^2} \exp\left(-\frac{P^2}{2\sigma_R^2}\right) \tag{3}$$

To eliminate the noise present in an image, it is important to estimate its quantity. It is well known that MRI images are often corrupted with Rician noise and various methods exist to estimate it. The most conventional and well known approach for such an estimation is to find the signal to noise ratio of the second order moment in a Rician distribution [7].
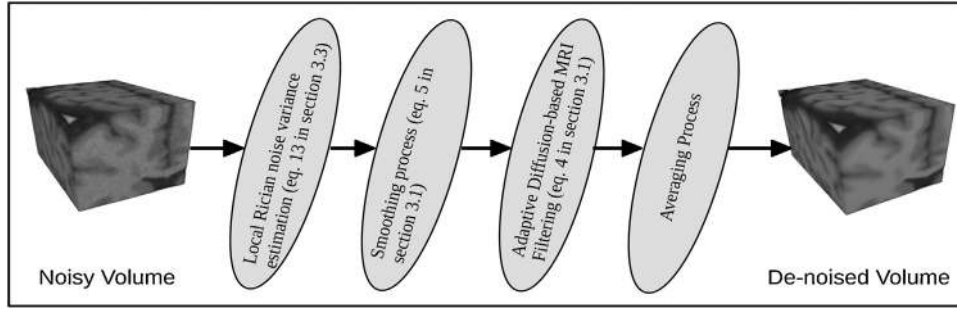
**Fig. 1.** Flow-diagram of the proposed ADMF3D algorithm.

The signal is estimated as: $N = \sqrt{\mu + 2\sigma_R^2}$, where $\mu$ is the order of moment. Some state of the art approaches like NLM [13], *maximum likelihood estimation* (ML) [41] exists based on the random nature of the Rician noise. Among them, one of the techniques namely *linear minimum mean square error* (LMMSE) [9] used by Aja-Fernández is worth mentioning. Some moment based estimation techniques with multiple order do exist. First order moment, based on Rayleigh distribution as shown in Eq. (3), uses noise standard deviation. Second order moment based Rician noise estimation has been recently used [18]. Coupé [42] proposed a wavelet based median absolute deviation (MAD) estimator for Rician noise with $\sigma_R = \frac{MAD(\|Y\|)}{0.6745}$ and $\hat{\sigma}_R = \sqrt{\sigma_R/\zeta(\theta)}$ where $Y$ is the wavelet coefficients of the HHH sub-band, HHH denotes the high sub-bands, $\theta$ is the SNR value and $\zeta$ is the correction factor [43].

Generally, estimation methodology can be grouped into two broad categories namely, background and object based. Background based method works in assumption that the background is void of any information (i.e. no signal) and the object based method assumes the presence of Gaussian noise mixed with the object under consideration.

However, these methodologies are more prone to error insertion, since they are approximation based. Therefore, as an alternative solution we propose a novel methodology which computes local Rician variance based on second order moment, irrespective of background and object (which is Gaussian noise in complex domain in MRI images).

## 3. Proposed methodology

### 3.1. Adaptive diffusion-based MRI filter

Our primary concern related to MRI filtering is to remove Rician noise without disturbing the edge and texture information. To filter the noise, we focused on solving global anisotropic diffusion function with gradient descent. Our proposed adaptive diffusion-based MRI filter (ADMF3D) is expressed as:

$$I^{t+1} = I^t + \frac{\lambda}{n} \sum_{d \in n} \Psi(IV_d, \sigma) \qquad (4)$$

where $I^t$ denotes the input image, $\lambda$ is the constant which determines the rate of diffusion, $n$ denotes the number of neighborhood pixels, $t$ is the distinct time step, $\Psi$ denotes the our proposed influence function (described in Section 3.2) and $\sigma$ is a scaling parameter. An automatic tuning of smoothing process makes it adaptive in nature.

$IV_d$ in Eq. (4) is the result of element wise multiplication between local Rician variance $Var(P)$ (computational description
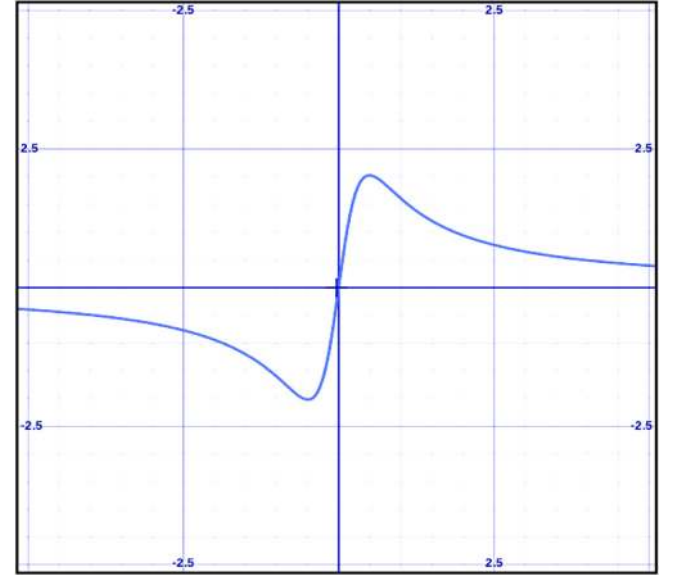


**Fig. 2.** Anisotropic diffusion influence (i.e. *g* stopping) function plot, based on Lorenzian error norm.

provided in Section 3.3) and the difference between central ($I_d$) and its neighboring pixels ($I_d - I^t$) expressed as:

$$IV_d = \sum_{d \in n} Var(P) \odot (I_d - I^t) \qquad (5)$$

The difference computing module (gradient) in Eq. (5) generates value of very low magnitude, even zero mean in homogeneous regions (by normal distribution even at regions with noise and no edges) but would generate spikes at intensity discontinuities (heterogeneous regions) [44]. This helps to find out the boundaries of lobes in the images. This also helps in diffusing the normally distributed noise. However, in presence of Rician noise, influence function should include the information of the properties of the noise. To achieve this, we perform an element-wise multiplication with $Var(P)$ and ($I_d - I^t$). The behavioral change of influence function $\Psi$ as a result of element-wise multiplication will be comprehensible after its character analysis.

### 3.2. Proposed influence function

While denoising there is a need to stop over-smoothing of the averaging process, which blurs the denoised image. The graph shown in Fig. 2 does not converge at either ends, and can lead to over-smoothing if executed over multiple iterations. Thereby, as a solution to this problem we introduce a statistical edge stopping function (influenced by Tukey's concept) to well converge/stop
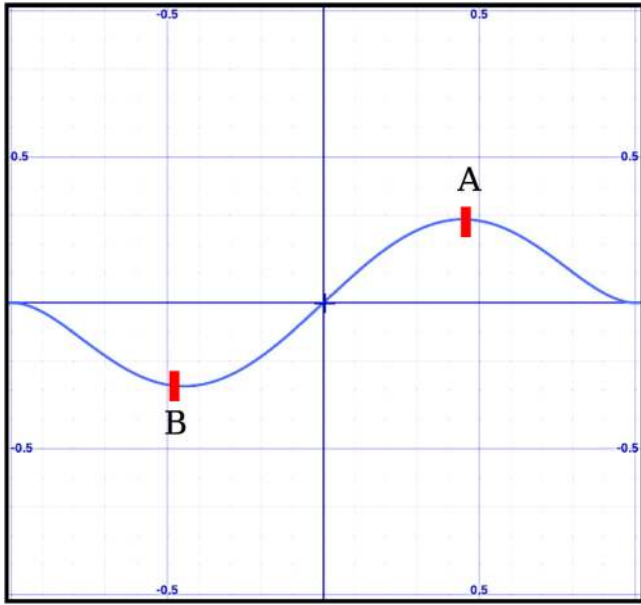
**Fig. 3.** Proposed edge stopping function with stationary points A and B.

the smoothening process at both ends as shown in Fig. 3 [45]. The nature of the influence function $\Psi$ is as shown in Eq. (6):

$$\Psi(x, \sigma) = \begin{cases} x\left[1 - (x/\sigma)^2\right]^2 & x \leq \sigma, \\ 0, & otherwise \end{cases} \tag{6}$$

where $x = IV_d$ as given in Eq. (5).

Further analysis of the biweight $\Psi$ function would make things more transparent. In Eq. (4) this biweight function is used as an edge stopping function.

The main reason to choose this function, is due to its rapid convergence by putting a stop to the averaging process.

If we see the conventional anisotropic diffusion's influence function (i.e. $g$ stopping),

$$g(x) = x.e^{-(x^2/k^2)} \tag{7}$$

where $k$ is a small constant. This is also proportional to the Lorenzian error norm. The first order derivative of Eq. (7) has been plotted in Fig. 2.

Again the plot of the first order derivative of the biweight function expressed in Eq. (6) has been shown in Fig. 3.

On comparing the nature of the graphs generated from Eqs. (6) and (7) (i.e. the first order derivative plots shown in Fig. 4), it is observed that the proposed edge stopping function put a stop to averaging process more rapidly. This helps in preserving more accurately the fine textures in the images. For knowing the effectiveness of this function, we examine it on some normal (peppers) images as shown in Fig. 5, where background has been added as a black patch together with a uniform Rician noise with ($\sigma_R = 9\%$).

From the previous expressions, it is well observed that the influence function $\Psi$ also depends on the *scaling parameter $\sigma$* of an image, and can be defined by means of statistical scale measures as expressed below [46]:

$$\begin{aligned} \sigma_s &= p \times MAD(\nabla I) \\ &= p \times median(||\nabla I - median(||\nabla I||)||) \end{aligned} \tag{8}$$

where $p$ is the scale factor, for normal distribution it is well known that $p \approx 1.4826$ where *MAD* denotes the *median absolute deviation* and the constant is derived from the fact that the MAD of a zero-mean normal distribution (Gaussian) with unit variance is 0.67449.
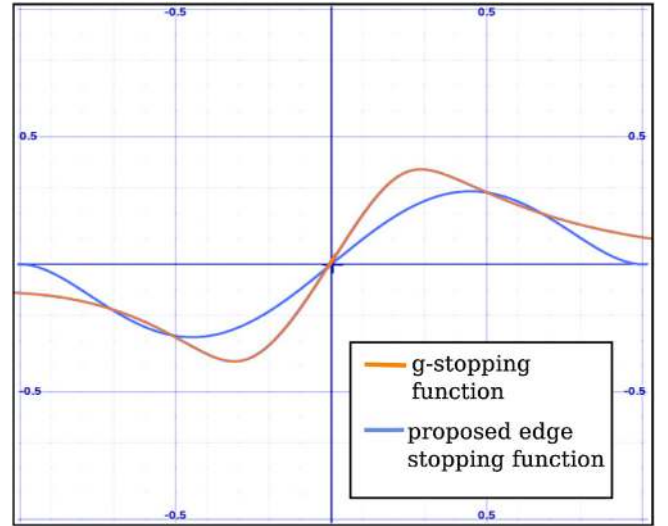


**Fig. 4.** Comparison plot between $g$ stopping function and proposed edge stopping function.

The value of *scaling parameter $\sigma$*, for the proposed biweight function norm is, $\sigma_s = \sigma\sqrt{5}$ [33] which is obtained from the stationary points (curvature starts decreasing or increasing gradually) of the influence function shown in Fig. 3 (points A, B).

### 3.3. Local variance based estimator

In general almost all noise estimation techniques are based on noise variance present in an image. Global noise estimation techniques did not prove to be an efficient parameter for denoising.

In this section, we propose a local variance based noise estimation methodology. The raw moment of rice distribution can be expressed with confluent hyper-geometric equation given by [47]:

$$E[P] = \left(2\sigma_R^2\right)^{\mu/2} \Gamma\left(\frac{\mu}{2} + 1\right) {}_1F_1\left[-\frac{\mu}{2}; 1; -\frac{m^2}{2\sigma_R^2}\right] \tag{9}$$

where $\mu$ is the order of moment, $\Gamma$ denotes gamma function, and ${}_1F_1$ is the confluent hyper-geometric function of the first kind. $m$ and $\sigma_R$ has already been mentioned in the theoretical background section. The first moment $E[P_1]$, and the second moment $E[P_2]$ of rice probability distribution are expressed in Eqs. (10) and (11) respectively as [48,49]:

$$E[P_1] = \sigma_R\sqrt{\frac{\pi}{2}} e^{-m^2/4\sigma_R^2} \left[\left(1 + \frac{m^2}{2\sigma^2}\right) I_0\left(\frac{m^2}{4\sigma_R^2}\right) + \frac{m^2}{2\sigma_R^2} I_1\left(\frac{m^2}{4\sigma_R^2}\right)\right] \tag{10}$$

and

$$E[P_2] = m^2 + 2\sigma_R^2 \tag{11}$$

where $I_0$ is the zeroth order modified Bessel function of the first kind, $I_1$ is the first order modified Bessel function of first kind and $m$ is the magnitude. To estimate the noise, we focused on the second central moment, the Rician variance, given by [43,50]:

$$\begin{aligned} Var(P) &= E[P_2] - E[P_1]^2 \\ &= m^2 + 2\sigma_R^2 - \frac{\pi\sigma_R^2}{2} e^{-m^2/2\sigma_R^2}\left[\left(1 + \frac{m^2}{2\sigma_R^2}\right) I_0\left(\frac{m^2}{4\sigma^2}\right)\right. \\ &\quad \left. + \frac{m^2}{2\sigma_R^2} I_1\left(\frac{m^2}{4\sigma_R^2}\right)\right]^2 \end{aligned} \tag{12}$$
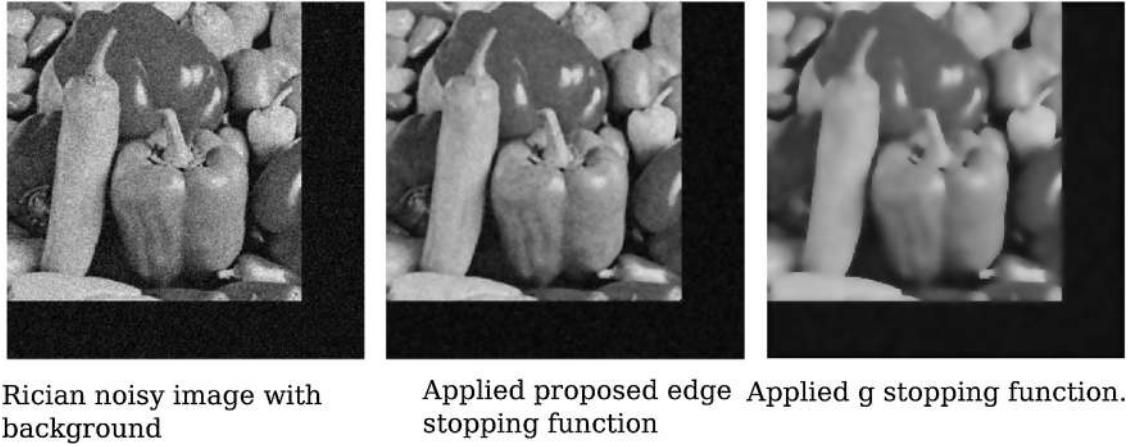
**Fig. 5.** Comparison between proposed edge stopping function and *g* stopping function on normal image, (left) Rician noisy ($\sigma_R = 9\%$) image with added background, (middle) applied proposed biweight function and (right) applied *g* stopping function.

The raw moment, the Rician variance $Var(P)$, can be expressed in more simple way using Laguerre polynomial [41,47], which equates to:

$$Var(P) = m^2 + 2\sigma_R^2 - \frac{\pi\sigma_R^2}{2}L_{1/2}\left(\frac{-m^2}{2\sigma_R^2}\right) \tag{13}$$

where $L_{1/2}(q)$ denotes a Laguerre polynomial of order 1/2 and $L_{1/2}$ is given by:

$$L_{1/2}(q) = e^{q/2}\left[(1-q)I_0\left(\frac{-q}{2}\right) - qI_1\left(\frac{-q}{2}\right)\right] \tag{14}$$

where $q = (\frac{-m^2}{2\sigma_R^2})$.

Low resolution kernel assists well to accurately estimate the local noise at the cost of a delta increase in computational burden, in contrast to large size kernels. Hence, we have taken $(3 \times 3 \times 3)$ kernel resolution for Rician noise estimation while scanning through the image. The complete steps of our proposed methodology has been summarized as shown in Algorithm 1 1 in Section 3.3.

**Algorithm 1.** Adaptive diffusion-based MRI filter

---

**Input:** Noisy MRI volume data $I^t$.
**Output:** Denoised MRI volume data $I^F$.
$-----$**Local variance based estimator**$-----$
1:      Estimate the local Rician noise of MRI volume data $I^t$ based on second order moment (variance) $Var(P)$.
2:      **for** the entire volume $I^t$ **do**
3:         Compute the local Rician variance with kernel size $(3 \times 3 \times 3)$.
4:         $Var(P) = m^2 + 2\sigma_R^2 - \frac{\pi\sigma_R^2}{2}L_{1/2}\left(\frac{-m^2}{2\sigma_R^2}\right)$ according to (12)
5:      **end for**
$-----$**Adaptive Diffusion-based 3D MRI Filter**$-----$
6:      **for** $t = 1$ to $n$ no of iteration **do**
7:         Compute $(I_d - I^t)$, difference between central and its neighboring pixels (26 neighbors).
8:         $IV_d = \sum_{d \in n} Var(P) \odot (I_d - I^t)$ according to (5)
9:         $I^{t+1} = I^t + \frac{\lambda}{n}\sum_{d \in n} \Psi(IV_d, \sigma)$ according to (4)
10:      **end for**
11:      Restore MRI via averaging all the volumetric data, by: $I^F = Median(I^{tn})$.
12:      **return** $I^F$

---

## 4. Experimental results

This section contains the results performed on synthetic (3D), and real MRI data. We have conducted our experiments using *MATLAB$^{TM}$* R2018b 64-bit software on Intel processor Core i7-880 @3.20GHz with Linux Ubuntu 16.04 operating system.
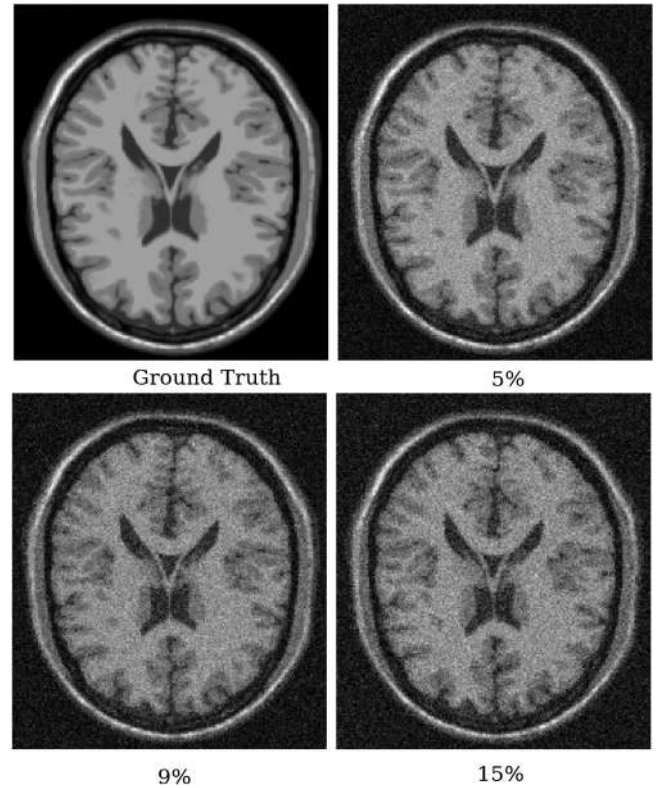


**Fig. 6.** Synthetic MRI data from BrainWeb blended with Rician noise in different noise level, top left: ground truth; top right: Rician noise – 5%; bottom left: Rician noise – 9% and bottom right: Rician noise – 15%.

### 4.1. Experiments on simulated/synthetic dataset

To verify our proposed methodology we have conducted experiments on synthetic MRI images obtained from BrainWeb, URL: http://www.bic.mni.mcgill.ca/brainweb [51]. Denoising performance has been evaluated by inserting Rician noise with different values of standard deviation ranging from $\sigma_R = 3\%–17\%$ (2% increment at every step). Three different types of weighted images namely T1-weighted, T2-weighted and PD-weighted normal brain MRI with $(181 \times 217 \times 181)$ dimension is used for experimentation. Fig. 6 shows the synthetic MRI ground truth data blended with different noise levels from 5% to 15%.

### 4.2. Evaluation based on the following performance metrics on simulated data

We evaluated our results with the reference dataset from brain-web, T1 T2 and PD-weighted normal brain MRI data ($181 \times 217 \times 181$) based on RMSE, PSNR and SSIM evaluation metrics. The Root Mean Square Error (RMSE) [52] metric is the most conventional way for pixel-to-pixel error measurement, given by,

$$RMSE = \sqrt{\frac{1}{n}\sum_{i=1}^{n}(\hat{y}_i - y_i)^2} \qquad (15)$$

where $\hat{y}_i$ is the input image and $y_i$ is output image and $n$ is the sample value for the MSE estimate. The image dimension is ($181 \times 217 \times 181$) for $n$.

Secondly, peak signal to noise ratio (PSNR) is the metric used to compare image compression quality expressed as, $PSNR = 10\log_{10}\left(\frac{M^2}{MSE}\right)$ where $M$ the maximum possible pixel value of the image and MSE is the means square error.

Based on the structural information of the image, another significant evaluation metric called Structural Similarity (SSIM) has been introduced by Wang et al. [53]. In this approach the structural similarity between the two input images namely the ground truth $x$ and the denoised image $y$ is computed and is expressed as:

$$SSIM(x, y) = \frac{(2\eta_x\eta_y + C_1)(2\sigma_{xy} + C_2)}{(\eta_x^2 + \eta_y^2 + C_1)(\sigma_x^2 + \sigma_y^2 + C_2)} \qquad (16)$$

where $C_1$ and $C_2$ are constants, $\sigma$ standard deviation and $\eta$ is mean intensity.

### 4.3. Performance evaluation on simulated dataset

We have compared our proposed *adaptive diffusion-based MRI filter (ADMF)* methodology, with the following benchmark methodologies as shown in Table 1 and have compared based on the evaluation metrics described in Section 4.2. All the quantitative and qualitative analysis have been shown in Tables 1, 2, 3, and in Figs. 7–11 respectively. Tables 1, 2, 3 shows the quantitative comparative analysis with respective to some benchmark methodologies in presence of Rician noise standard deviation ranging from 3% to 17%. Our proposed methodology outperformed all other methodologies in most of the cases. Our methodology has been compared with the following state-of-the-art works as itemized below.

**Table 1**
Comparison of the performance of denoising techniques based on the quantitative metrics in different levels of Rician noise for the T1-weighted synthetic MRI volume. The bold values indicate the best results in comparison with the other studies.

| $\sigma_R$ | 3% | | 5% | | 7% | | 9% | | 11% | | 13% | | 15% | | 17% |
|---|---|---|---|---|---|---|---|---|---|---|---|---|---|---|---|
| | SSIM | PSNR | SSIM | PSNR | SSIM | PSNR | SSIM | PSNR | SSIM | PSNR | SSIM | PSNR | SSIM | PSNR | SSIM | PSNR |
| Noisy | 0.81 | 30.49 | 0.66 | 26.02 | 0.52 | 23.09 | 0.44 | 21.04 | 0.36 | 19.19 | 0.31 | 17.71 | 0.25 | 16.45 | 0.23 | 15.39 |
| BM4D [25] | 0.98 | 38.34 | 0.96 | 36.28 | 0.94 | 34.59 | 0.92 | 33.34 | 0.90 | 32.38 | 0.88 | 31.54 | 0.86 | 30.83 | 0.84 | 30.08 |
| LTA3D [16] | 0.98 | 38.52 | 0.96 | 36.78 | 0.95 | 35.10 | 0.93 | 33.71 | 0.92 | 32.63 | 0.90 | 32.16 | 0.88 | 31.38 | 0.85 | 30.67 |
| RNOLMMSE [22] | 0.95 | **38.64** | 0.94 | **36.72** | 0.93 | 34.16 | 0.92 | 33.17 | 0.90 | 32.44 | 0.88 | 31.27 | 0.87 | 30.43 | 0.85 | 29.93 |
| MNL-tSVD [29] | 0.98 | 38.27 | 0.96 | 36.37 | 0.94 | **35.28** | 0.92 | 33.66 | 0.90 | 32.74 | 0.89 | **32.34** | 0.88 | 31.67 | 0.86 | 30.58 |
| PRINLM3D [13] | 0.98 | 38.19 | 0.96 | 35.34 | 0.94 | 33.37 | 0.92 | 32.14 | 0.89 | 30.88 | 0.87 | 30.15 | 0.85 | 29.72 | 0.83 | 29.26 |
| ROLMMSE [20] | 0.97 | 38.13 | 0.96 | 35.87 | 0.93 | 33.74 | 0.90 | 32.53 | 0.88 | 31.54 | 0.86 | 30.43 | 0.85 | 30.06 | 0.83 | 29.53 |
| ADMF3D | 0.98 | 38.08 | 0.96 | 36.12 | 0.95 | 34.78 | **0.94** | **33.74** | 0.92 | **32.86** | **0.91** | 32.28 | **0.89** | **31.44** | **0.87** | **30.86** |

**Table 2**
Comparison of the performance of denoising based on the quantitative metrics in different levels of Rician noise for the T2-weighted synthetic MRI volume. The bold values indicate the best results in comparison with the other studies.

| $\sigma_R$ | 3% | | 5% | | 7% | | 9% | | 11% | | 13% | | 15% | | 17% |
|---|---|---|---|---|---|---|---|---|---|---|---|---|---|---|---|
| | SSIM | PSNR | SSIM | PSNR | SSIM | PSNR | SSIM | PSNR | SSIM | PSNR | SSIM | PSNR | SSIM | PSNR | SSIM | PSNR |
| Noisy | 0.86 | 29.57 | 0.76 | 25.35 | 0.65 | 22.86 | 0.58 | 21.42 | 0.52 | 19.64 | 0.48 | 17.18 | 0.43 | 16.47 | 0.38 | 15.27 |
| BM4D [25] | 0.97 | 37.67 | 0.95 | 35.16 | 0.93 | 32.24 | 0.90 | 30.88 | 0.88 | 29.94 | 0.86 | 28.42 | 0.84 | 27.15 | 0.82 | 26.23 |
| LTA3D [16] | 0.98 | 37.69 | 0.96 | 35.27 | 0.94 | 32.41 | 0.92 | 31.07 | 0.91 | 30.22 | 0.90 | 28.64 | 0.88 | 27.38 | 0.85 | 26.52 |
| RNOLMMSE [22] | 0.95 | **37.92** | 0.94 | 34.26 | 0.93 | 32.52 | 0.91 | 31.14 | 0.89 | 29.75 | 0.87 | 28.42 | 0.85 | 27.35 | 0.84 | 26.25 |
| MNL-tSVD [29] | 0.98 | 37.25 | 0.96 | **35.67** | **0.95** | 32.76 | 0.93 | **31.57** | 0.91 | 30.16 | 0.90 | **28.76** | 0.88 | 27.53 | 0.86 | **26.67** |
| PRINLM3D [13] | 0.98 | 36.72 | 0.96 | 34.14 | 0.94 | 32.34 | 0.92 | 30.84 | 0.90 | 29.63 | 0.88 | 27.55 | 0.85 | 26.07 | 0.83 | 25.18 |
| ROLMMSE [20] | 0.97 | 36.86 | 0.95 | 34.06 | 0.93 | 31.85 | 0.92 | 30.57 | 0.90 | 29.25 | 0.88 | 27.76 | 0.87 | 26.82 | 0.84 | 25.46 |
| ADMF3D | 0.98 | 37.87 | 0.96 | 35.44 | 0.94 | **32.90** | **0.93** | 31.46 | **0.92** | **30.28** | **0.91** | 28.64 | **0.89** | **27.78** | **0.87** | 26.54 |

**Table 3**
Comparison of denoising techniques based on the quantitative metrics in different levels of Rician noise for the PD-weighted synthetic MRI image. The bold values indicate the best results in comparison with the other studies.

| $\sigma_R$ | 3% | | 5% | | 7% | | 9% | | 11% | | 13% | | 15% | | 17% |
|---|---|---|---|---|---|---|---|---|---|---|---|---|---|---|---|
| | SSIM | PSNR | SSIM | PSNR | SSIM | PSNR | SSIM | PSNR | SSIM | PSNR | SSIM | PSNR | SSIM | PSNR | SSIM | PSNR |
| Noisy | 0.79 | 30.86 | 0.64 | 27.16 | 0.52 | 23.46 | 0.42 | 21.28 | 0.37 | 19.24 | 0.32 | 17.56 | 028 | 16.08 | 0.25 | 14.88 |
| BM4D [25] | 0.97 | 38.18 | 0.94 | 35.67 | 0.92 | 34.06 | 0.89 | 32.24 | 0.86 | 31.22 | 0.83 | 29.85 | 0.81 | 29.14 | 0.78 | 28.25 |
| LTA3D [16] | **0.98** | 38.44 | 0.96 | 36.12 | 0.94 | 34.32 | 0.93 | 32.58 | 0.91 | **31.86** | 0.89 | 30.24 | 0.88 | 29.37 | 0.87 | 28.56 |
| RNOLMMSE [22] | 0.94 | 37.55 | 0.92 | 35.36 | 0.88 | 32.44 | 0.85 | 31.54 | 0.84 | 30.68 | 0.82 | 29.76 | 0.81 | 28.95 | 0.80 | 28.17 |
| MNL-tSVD [29] | 0.97 | **38.76** | 0.96 | 36.22 | 0.94 | **34.57** | 0.93 | 32.47 | 0.91 | 31.64 | 0.89 | **30.87** | 0.88 | 29.62 | 0.86 | 28.86 |
| PRINLM3D [13] | 0.97 | 37.24 | 0.95 | 35.17 | 0.92 | 32.74 | 0.89 | 31.87 | 0.87 | 30.73 | 0.85 | 29.08 | 0.82 | 28.18 | 0.79 | 27.07 |
| ROLMMSE [20] | 0.96 | 38.27 | 0.94 | 36.27 | 0.92 | 33.08 | 0.90 | 32.13 | 0.88 | 31.07 | 0.86 | 29.22 | 0.84 | 28.07 | 0.82 | 27.36 |
| ADMF3D | 0.97 | 38.56 | 0.96 | **36.27** | 0.94 | 34.36 | 0.93 | **32.65** | **0.92** | 31.75 | **0.90** | 30.78 | **0.89** | **29.73** | 0.87 | **28.92** |
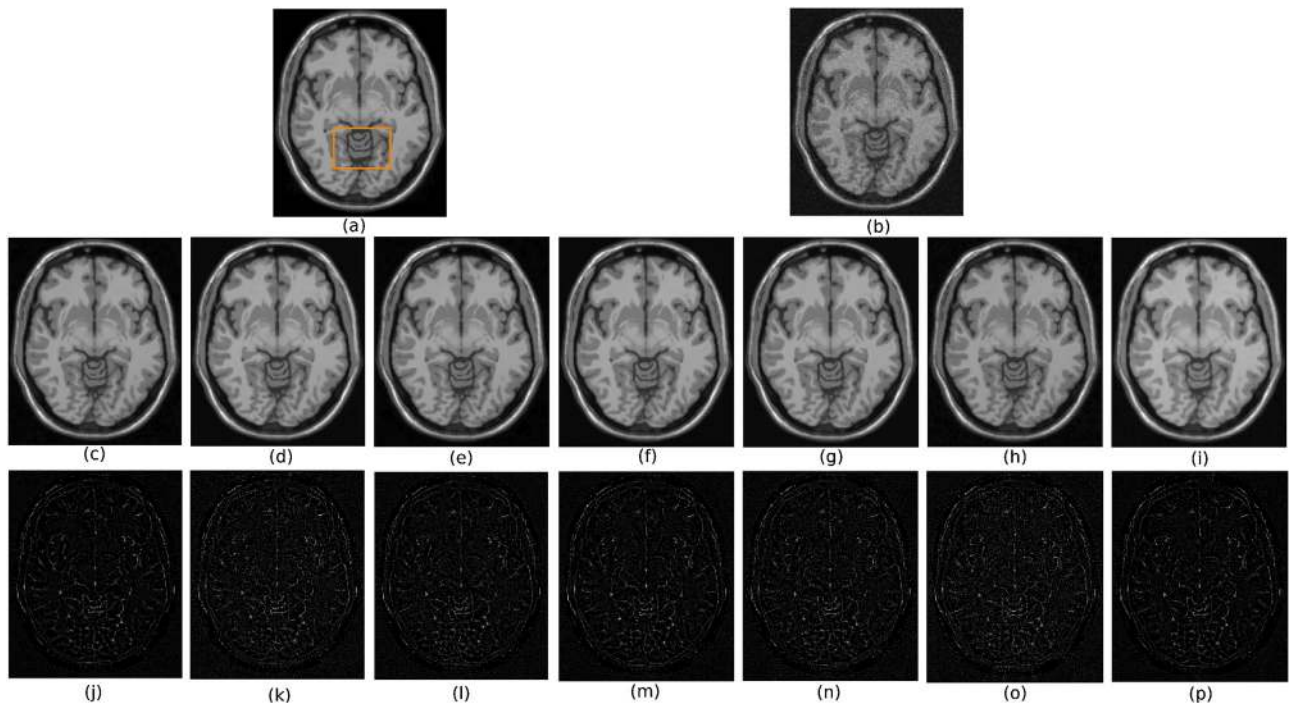
**Fig. 7.** Example filtering results for an axial slice of the T1-w BrainWeb phantom (Rician noise level of 9%). (a) Original image, (b) noisy image, (c)–(i) refers to the methodologies starting from BM4D to ADMF3D as shown in Table 1. The third row shows the absolute value of the image residuals for the different methods.
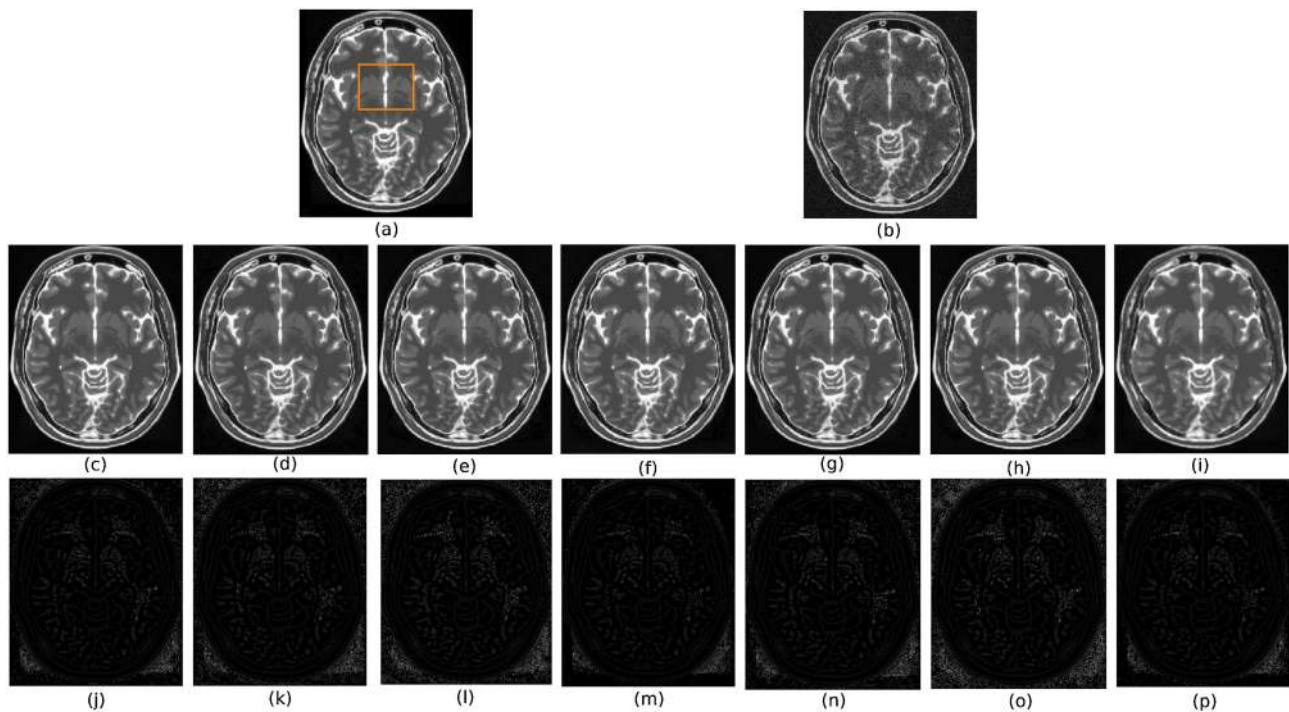


**Fig. 8.** Example filtering results for an axial slice of the T2-w BrainWeb phantom (Rician noise level of 9%). (a) Original image, (b) noisy image, (c)–(i) refers to the methodologies starting from BM4D to ADMF3D as shown in Table 1. The third row shows the absolute value of the image residuals for the different methods.

- The nonlocal transfer-domain filter (BM4D) proposed by Maggioni et al. [25].
- The Low-rank tensor approximation for 3D MRI filter (LTA3D) was proposed by Fu and Dong [16].
- MRI denoising based on modified LMMSE estimator for 3D MRI (RNOLMMSE) proposed by Yaghoobi and Hasanzadeh [22].

- 4D Nonlocal transform-domain filter for 3D MRI (MNL-tSVD) was proposed by Kong et al. [29].
- Sparseness and self-similarity based NLM filter for 3D MRI (PRINLM3D) was proposed by Manjón et al. [13].
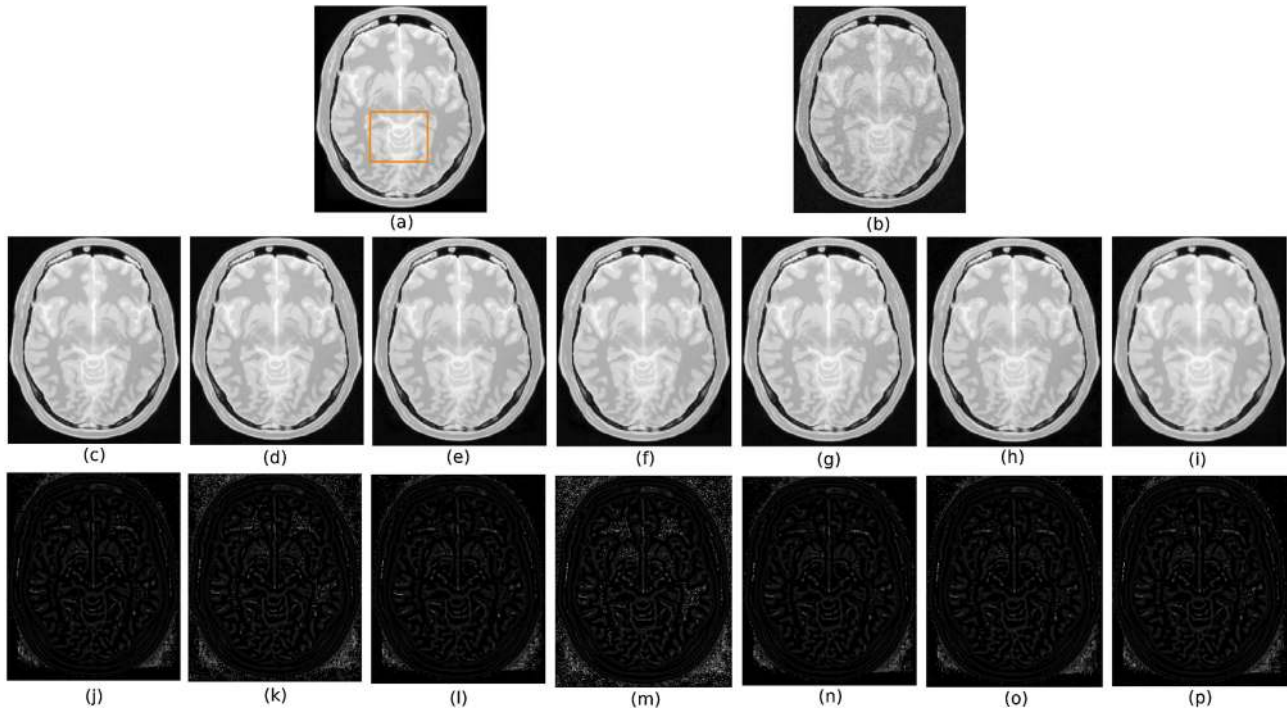- Optimized LMMSE based denoising for 3D MRI (ROLMMSE) was proposed by Golshan and Hasanzadeh [20].

**Fig. 9.** Example filtering results for an axial slice of the PD-w BrainWeb phantom (Rician noise level of 9%). (a) Original image, (b) noisy image, (c)–(i) refers to the methodologies starting from BM4D to ADMF3D as shown in Table 1. The third row shows the absolute value of the image residuals for the different methods.
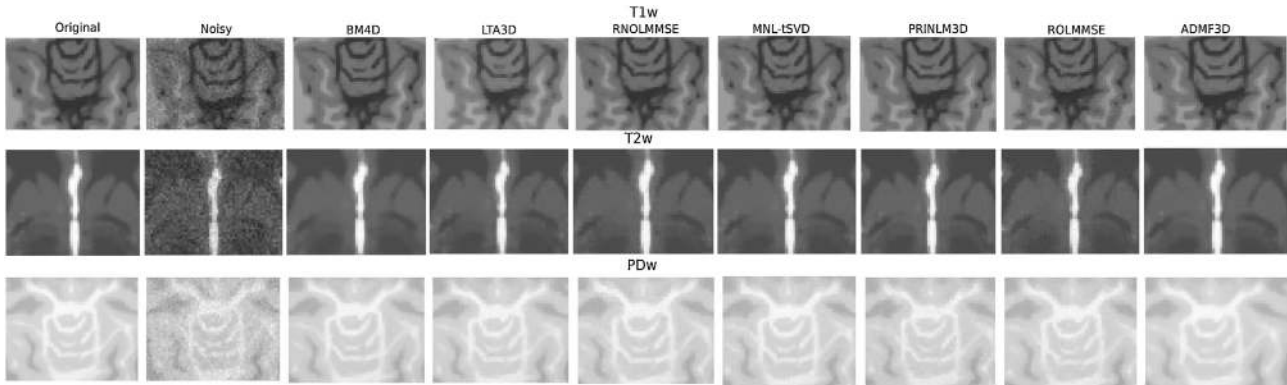


**Fig. 10.** Example filtering results for region of interest cut (zoom view) of T1-w, T2-w and PD-w BrainWeb phantom (Rician noise level of 9%).

The results for denoising with different values of $\sigma_R$ (ranging from 3% to 17%) for T1/T2/PD-weighted ($181 \times 217 \times 181$) normal brain images are shown in Tables 1, 2, 3. The results from Tables 1, 2, 3 has been plotted and shown in Fig. 12, and the analysis is as follows. Observation shows that LTA3D [16] and MNL-tSVD [29] outperforms us narrowly in few scenarios mostly in low noise range.

MNL-tSVD [29] produces very comparable performance with our's in respect to signal to noise ratio and even exceeds in the noise range of 12–15 standard deviation in T1-w weighted images (Fig. 12) but lags in SSIM metric in all the cases.

LTA3D [16] shows moderate structural similarity in mid-range noise ranges and also similar with us in certain points in the noise range of 7, 9, 11 and 17 in T1-w, T2-w and PD-w modality of images. Also it shows almost comparable performance with respect to signal to noise ratio in almost all noise ranges in T1 and T2-w. However, its performance of signal to noise ratio is poor in case of PD-w modality of images (via Fig. 12) in the significant noise range of 11–17.

RNOLMMSE [22] lags in SSIM and signal to noise ratio every cases of T1, T2 and PD-weighted images and for the complete range of noise standard deviation.

PRINLM3D [13] and ROLMMSE [20] are closely matching with each other in T2 and PD-w, however, they lag far behind with our proposed methodology for all the modalities and for the complete range of standard deviations of noise.

Our's produces better results even in places of degradation of contrast information due to incremental noise as shown in Figs. 9 and 10. The contrast information among different tissues is also visually much better preserved on the filtered images as shown in from Figs. 7, 8, 9.

The third rows for Figs. 7, 8, 9 shows the residual images as obtained by subtracting the original image with the denoised/filtered one with $\sigma_R = 9\%$.

Hardly any notable structural feature is found in the residual images in our proposed methodology. The lower amount of residue characterizes our ADMF3D solution is evident.
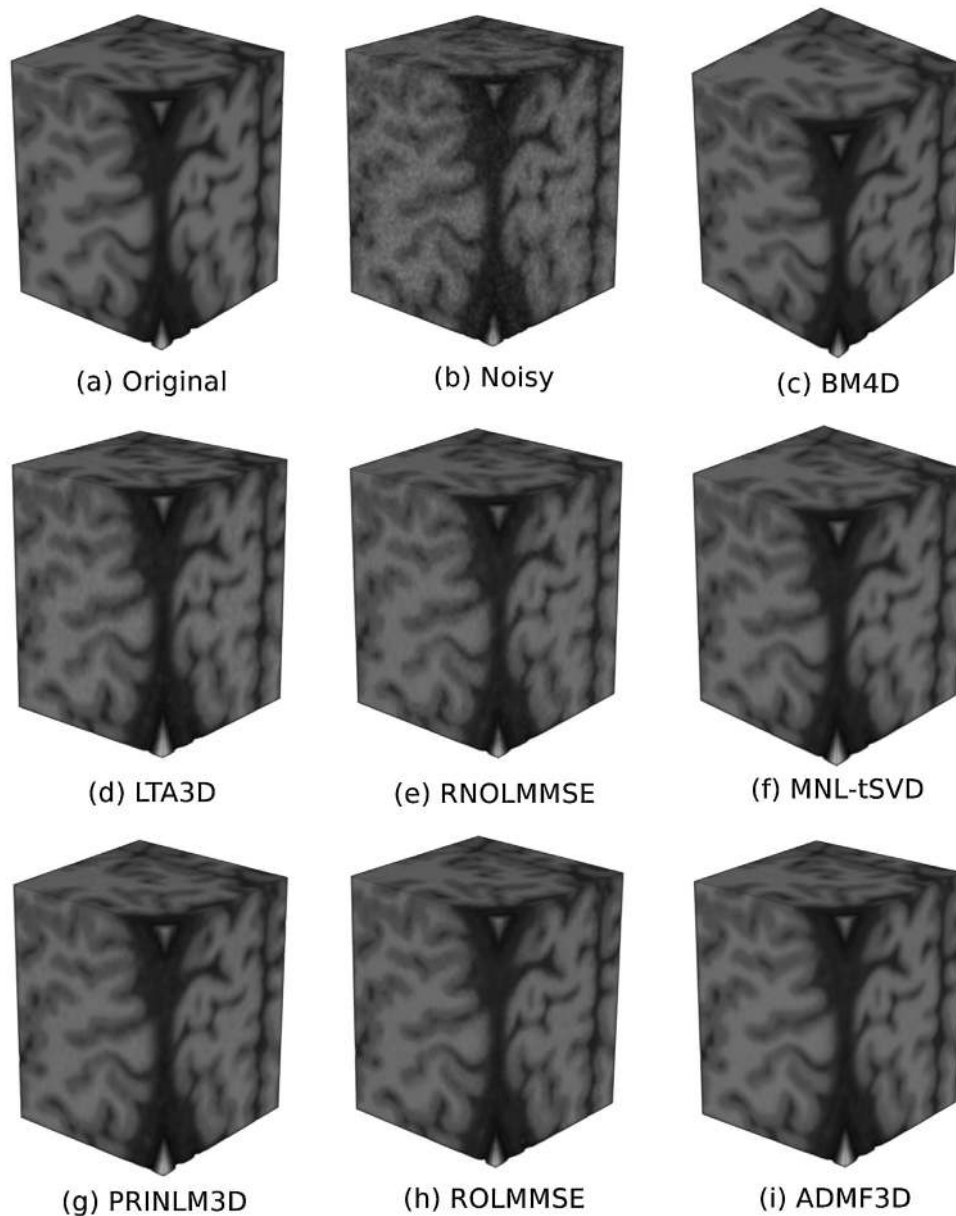
**Fig. 11.** Example filtering results volumetric view of T1-w BrainWeb phantom (Rician noise level of 9%).

Additionally, from the residual images of our proposed methodology, reveals that no meaningful anatomical information has been lost in the filtering process. The goodness of the denoised image is measured based on the zero intensity (black) values in the difference image. Higher zero intensity values signifies the closeness of the denoised image with that of the original image, which signifies the quality of the denoising methodology. Thus it is evident that our methodology performs better in accordance with the residual images in comparison to the other methodologies for Rician perturbed images. From the magnified view of the T1-w, T2-w and PD-w images as shown in (Fig. 10) as well as by the visual experience (with naked eye) it is well understood that the structural information and the fine textures are well preserved w.r.t. the comparing ones. We have evaluated their similarity by comparing the textures, using the distance metric like SSIM.

We further used the volumetric test data T1 BrainWeb phantom of size ($60 \times 80 \times 60$) voxels having 1.2 mm slice thickness, without noise, and without intensity non-uniformity as shown in Fig. 11. Added synthetically generated Rician noise with standard deviation of 9% to it, and performed the denoising operations. Compared against all the benchmark methodologies. The quantitative and qualitative experimental results shows that our ADMF3D represents the state of the art in MR image denoising. Our proposed methodology has been evaluated with the three evaluation metrics namely SSIM, PSNR and RMSE. The behavior of these metrics for the 3 weighted images (namely T1-w, T2-w and PD-w) have been plotted against the Rician noise standard deviation ranging from 3% to 17% as shown in Fig. 12. It is to be noted that the plot for each evaluation metrics follows almost the same pattern of movement along the noise axis for all the three weighted images respectively, manifesting the behavioral consistency throughout for each weights.

To evaluate the robustness of our proposed methodology we examine with another benchmark numerical MR simulator known as MRiLab [54], a new comprehensive simulator for large-scale realistic MRI simulations. MRiLab combines realistic tissue modeling with numerical virtualization of an MRI system and scanning experiment. This enables the assessment of a broad range of MRI approaches including advanced quantitative MRI methods infer-
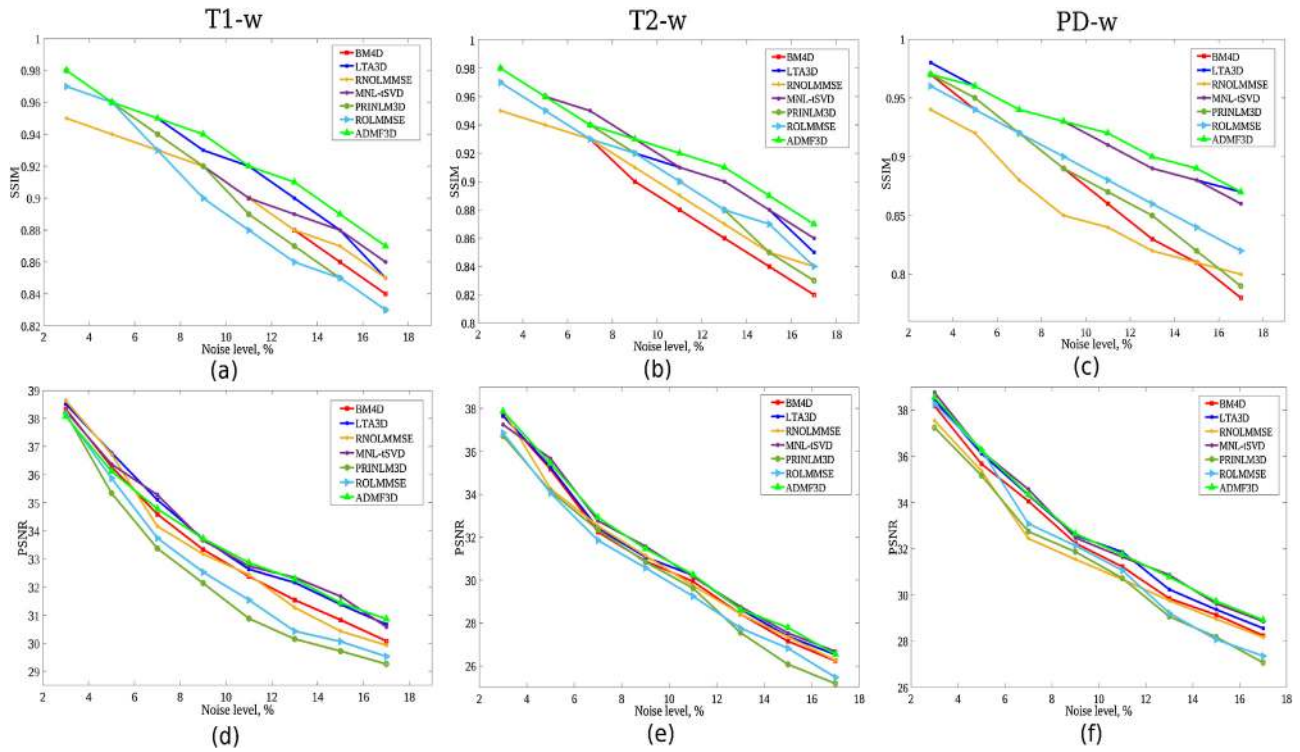
**Fig. 12.** SSIM and PSNR comparisons of ADMF3D with other denoising methodologies for the T1-w, T2-w and PD-w images under Rician noise levels varying from 3% to 17%. (a,b,c) shows the variance of SSIM with various noise level for T1-w, T2-w and PD-w images respectively. (d,e,f) shows the variance of PSNR with various noise level for T1-w, T2-w and PD-w images respectively.
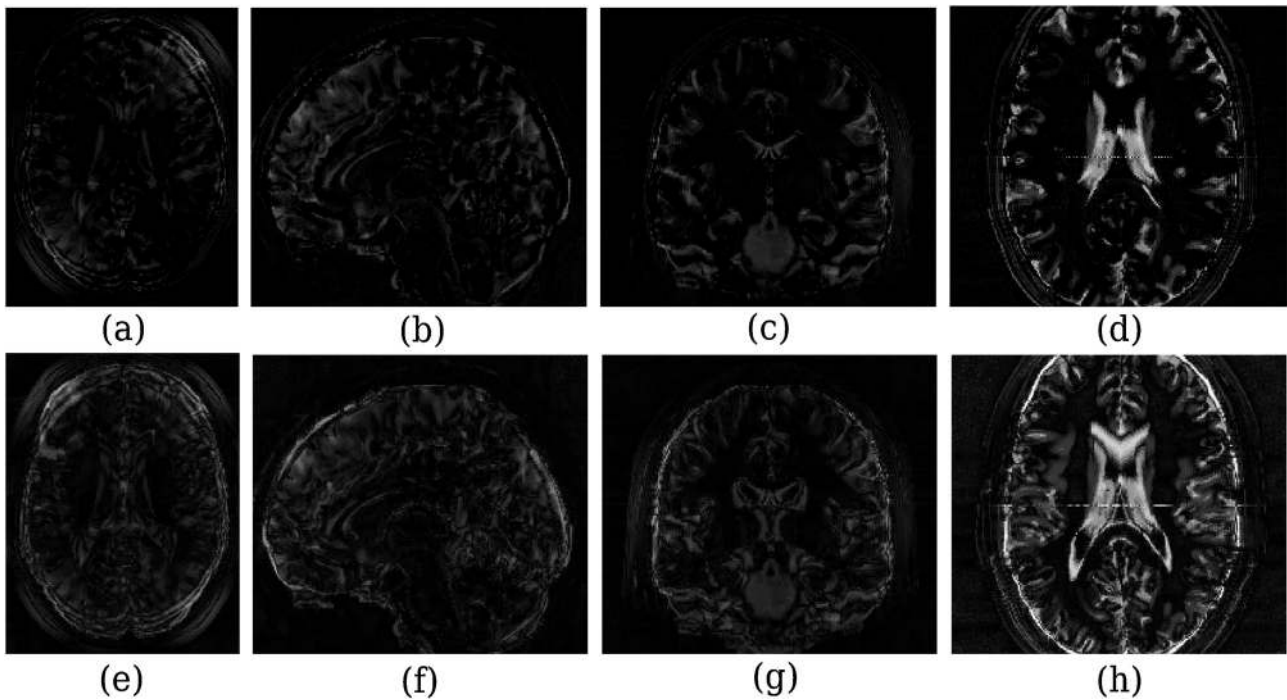


**Fig. 13.** Example showing the filtering results of MRiLab [54] simulated data for four different configuration. (a) Axial view, (b) sagittal view, (c) coronal view, (d) with *8-channel head SAR coil* axial view and (e)–(f) are the corresponding denoising results.

ring microstructure on a subvoxel level. The MRiLab software is available at http://mrilab.sourceforge.net/ for free open source access. In this study we have taken four different configuration of data (every volume size = 216 × 180 × 180 voxels, flip angle = 90° noise level 10% slice thickness=0.006 and multi-element coils (8-

channel head)). The filtering results for the four different MR simulated data are reported in Fig. 13. Visually it is observed that proposed ADMF3D performs well for multi-element coils MRI images, by preserving the fine edge information whilst maintaining the overall denoising quality.
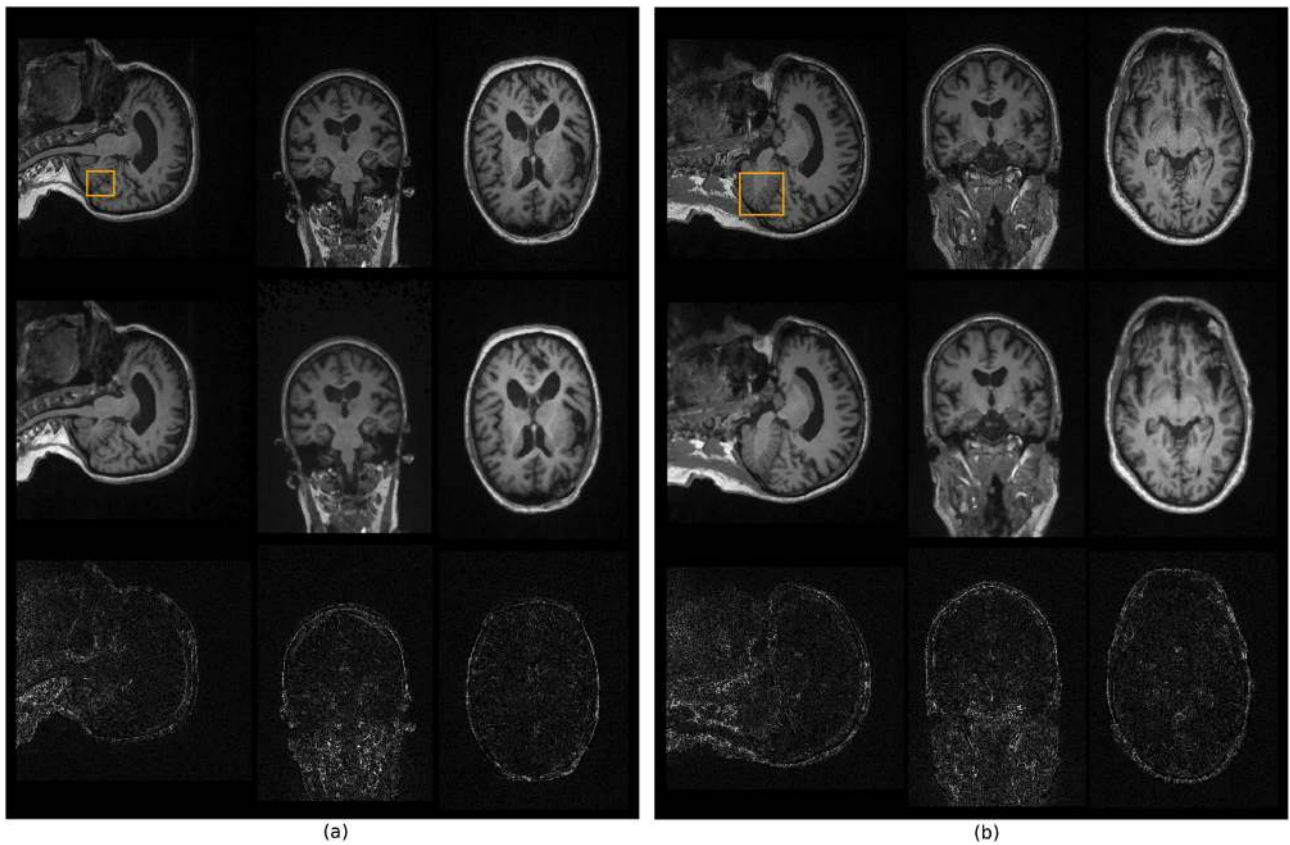
**Fig. 14.** Example results of the proposed ADMF3D filter on two sets of real brain data from OASIS [55]. From top to bottom: the first row shows the original observation, second row shows the denoised images and the corresponding residuals are shown in the third row respectively. (a) for TEST-I dataset and (b) for TEST-II dataset.
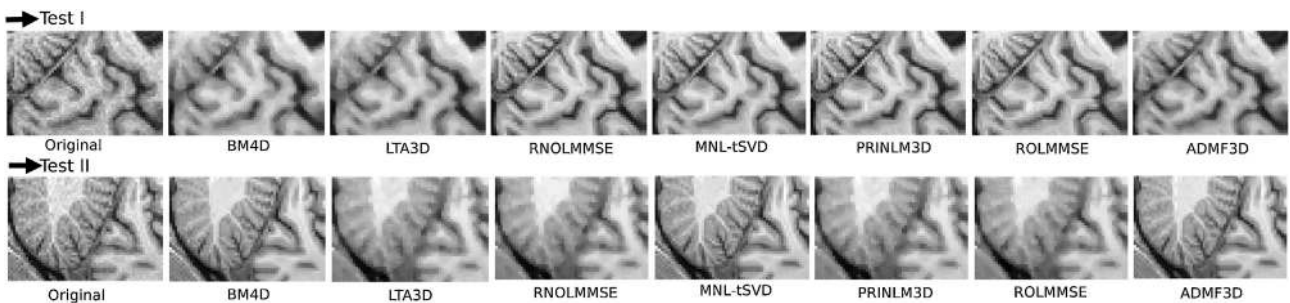


**Fig. 15.** Top, region of interest area cut for TEST-I dataset and bottom, region of interest cut for TEST-II dataset.

### 4.4. Experimentation on real MRI data

In this study, we have experimented with two real MRI datasets (namely OAS30573_MR_d0515 and OAS30766_MR_0147) from *Open Access Series of Imaging Studies* (OASIS) URL: http://www.oasis-brains.org [55]. The T1-weighted 3D MR volume (size = 256 × 240 × 176 voxels, flip angle = 9°, slice thickness = 1.2 mm, with repetition time = 2.3 ms, echo time = 0.00295 ms and inversion time = 0.9 ms) for coronal, axial and sagittal (Test-I and Test-II) has been obtained from Siemens Biograph-mMR MR-PET scanner, 3.0 T system respectively as shown in Fig. 14. A zoomed version has been taken as shown in a square box in the top row, and the denoised results has been shown in Fig. 15. We have applied several denoising filters namely BM4D, LTA3D, RNOLMMSE, MNL-tSVD, PRINLM3D and ROLMMSE (shown in Fig. 15) on Test-I and II respectively being shown in two corresponding rows. Few of them affects the image information and blurs the effective details of the image anatomical information, which plays a pivotal role in extracting the information for diagnosis. From a subjective point of view, ADMF3D achieves excellent visual results, as seen from the smoothness in flat areas. The details are preserved along the edges including the structural details, with better contrast and less blurring. Also an accurate restoration of the intensities in the phantom yields good-quality estimates.

### 4.5. Performance analysis

Comparative study regarding the execution time for various MRI denoising techniques are illustrated in Table 4. All experiments are carried out on a Quad Core Intel i7-880(R) CPU 3.20 GHz processor, 8 GB RAM in using MATLAB 2018b. From Table 4 it can be seen that ADMF3D produces more computationally efficient results with better visual effects in comparison to the benchmark studies like BM4D, LTA3D and MNL-tSVD, making it a suitable alternative for real MRI image denoising. Furthermore, our experimental observation states that 60% of computational cost of ADMF3D lies in the
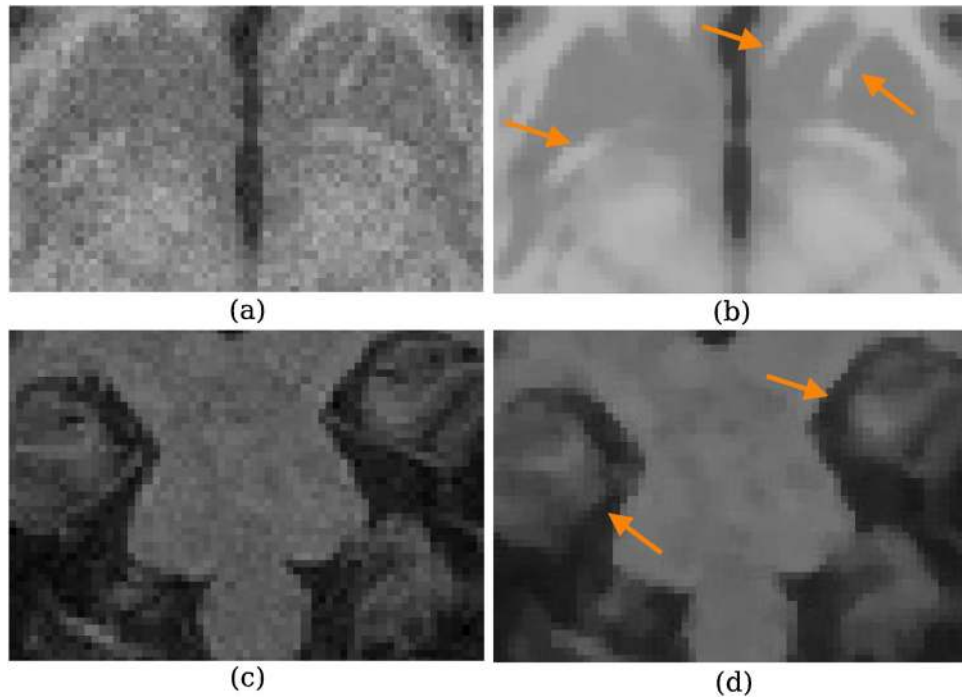
**Fig. 16.** Example denoising results of ADMF3D on T1w image corrupted with rician noise. (a) Synthetic T1w. (b) Filtered by ADMF3D. (c) Noisy real T1w. (d) Filtered by ADMF3D.

**Table 4**
Execution time comparison of different methods on simulated and real MRI data.

| Methods | Data | Execution time (min) |
| --- | --- | --- |
| BM4D | Simulated | 6.8 |
| | Real | 6.3 |
| LTA3D | Simulated | 8.5 |
| | Real | 8.3 |
| RNOLMMSE | Simulated | 0.72 |
| | Real | 0.78 |
| MNL-tSVD | Simulated | 7.4 |
| | Real | 6.6 |
| ROLMMSE | Simulated | 1.4 |
| | Real | 1.3 |
| PRINLM3D | Simulated | 1.2 |
| | Real | 1.0 |
| ADMF3D | Simulated | **3.4** |
| | Real | **2.2** |

Rician noise variance estimation, and our parallel implementation cuts down the overall computing time by half. Additionally, the efficiency can be further improved by simultaneously performing noise estimation and adaptive diffusion filtering.

Detailed results in the region of interest (foreground) are presented in Fig. 16. The figure shows the visual evaluation of magnified regions of the preserves anatomical structure (cranial nerves) after applying filter ADMF3D on synthetic and real T1w MRI images respectively. Our proposed filtering technique also preserve the details of cranial nerves accurately, making it a viable solution for a radiologist/clinician.

## 5. Conclusion

In this study, we have presented a novel filtering methodology that removes Rician noise from MRI by estimating the local noise variance, which drives the diffusion process of the filter. The adaptation of statistical edge stopping function captivates the preservation condition of anatomical structure of the MRI images.

We evaluated our proposed methodology with various types of T1-w, T2-w and PD-w MRI image data set and compared with the state-of-the-art methodologies. We have outperformed every other on the basis of structural similarity metric which proves that our proposed filter preserves very minutely the anatomical structure of images besides removing Rician noise. This ensures the essential objectives of medical image denoising for proper diagnosis. The signal to noise ration metric is comparable and also outperforms in few scenarios with the state-of-the-art approaches, denoting a proper denoising phenomenon too. The denoising methodology also performs well for the real dataset evident from the visual quality comparable to others. We also examine with another benchmark numerical MR simulator known as MRiLab, a new comprehensive simulator for large-scale realistic MRI simulations.

The well-known noise distributions in magnetic resonance imaging (MRI) data (Rayleigh, Rician, or non-central chi-distribution) describe the probability density of real-valued (i.e. floating-point) signal intensities. Our proposed methodology can reduced Rayleigh, Rician noise but needs improvement while removing noise generated from chi-distribution. Moreover, the performance of our methodology is average on MRI image affected with very low noise level. Our proposed implementation requires a computing time of 3.4 min for simulated dataset. For real MRI image the execution time is 2.2 min for a complete parallel implementation. We are in process of making our design more robust to handle larger size datasets w.r.t. resolutions and depth of the 3D MRI volume with reduced time of execution (by identifying the critical paths in the design flow) suitable for implementation in General Purpose Graphics Processing Unit (GPGPU).

**Declaration of Competing Interest**

Authors declare that they have no conflict of interest.

## References

[1] J. Mohana, V. Krishnavenib, Y. Guo, A survey on the magnetic resonance image denoising methods, Biomed. Signal Process. Control 9 (2014) 56–69.

[2] G. Gerig, O. Kubler, R. Kikinis, F.A. Jolesz, Nonlinear anisotropic filtering of MRI data, IEEE Trans. Image Process. 11 (1992) 221–232, http://dx.doi.org/10.1109/42.141646.

[3] J. Sijbers, J.A. den Dekker, A. der Linden, M. Verhoye, D. Van Dyck, Adaptive anisotropic noise filtering for magnitude MR data, Magn. Reson. Imaging 10 (1999) 1533–1539.

[4] G. McGibney, M.R. Smith, An unbiased signal-to-noise ratio measure for magnetic resonance images, Med. Phys. 20 (1993) 1077–1078, http://dx.doi.org/10.1118/1.597004.

[5] R.D. Nowak, Wavelet-based Rician noise removal for magnetic resonance imaging, IEEE Trans. Image Process. 8 (1999) 1408–1419, 1057-7149(99)07555-7.

[6] K. Krissian, Flux-based anisotropic diffusion applied to enhancement of 3-d angiogram, IEEE Trans. Med. Imaging 21 (2003) 1440–1442, http://dx.doi.org/10.1109/TMI.2002.806403.

[7] A. Buades, B. Coll, J. Morel, A non-local algorithm for image denoising, Comput. Vis. Pattern Recogn. 2 (2005) 60–65, http://dx.doi.org/10.1109/CVPR.2005.38.

[8] K. Krissian, C.F. Westin, R. Kikinis, K. Vosburgh, Oriented speckle reducing anisotropic diffusion, IEEE Trans. Image Process. 16 (2007) 1412–1424, http://dx.doi.org/10.1109/TIP.2007.891803.

[9] S. Aja-Fernández, C.A. Lopez, C.F. Westin, Noise and signal estimation in magnitude MRI and Rician distributed images: a LMMSE approach, IEEE Trans. Image Process. 17 (2008) 1383–1398, http://dx.doi.org/10.1109/TIP.2008.925382.

[10] J.V. Manjón, J. Caballero, J.J. Lull, G.G. Marti, L.M. Bonmati, M. Robles, MRI denoising using non-local means, Med. Image Anal. 12 (2008) 514–523, http://dx.doi.org/10.1016/j.media.2008.02.004.

[11] P. Coupé, P. Yger, S. Prima, P. Hellier, C. Kervrann, C. Barillot, An optimized blockwise nonlocal means denoising filter for 3-d magnetic resonance images, IEEE Trans. Med. Imaging 27 (2008) 425–441, http://dx.doi.org/10.1109/TMI.2007.906087.

[12] K. Krissian, S. Aja-Fernández, Noise-driven anisotropic diffusion filtering of MRI, IEEE Trans. Image Process. 18 (2009) 2265–2274, http://dx.doi.org/10.1109/TIP.2009.2025553.

[13] J.V. Manjón, P. Coupé, A. Buades, D. Collins, M. Robles, New methods for MRI denoising based on sparseness and self-similarity, Med. Image Anal. 16 (2012) 18–27, http://dx.doi.org/10.1016/j.media.2011.04.003.

[14] H.V. Bhujle, S. Chaudhuri, Laplacian based non-local means denoising of MR images with Rician noise, Magn. Reson. Imaging 31 (2013) 1599–1610, http://dx.doi.org/10.1016/j.mri.2013.07.001.

[15] H.M. Golshan, R.P. Hasanzadeh, S.C. Yousefzadeh, An MRI denoising method using image data redundancy and local SNR estimation, Magn. Reson. Imaging 31 (2013) 1206–1217, http://dx.doi.org/10.1016/j.mri.2013.04.004.

[16] Y. Fu, W. Dong, 3d magnetic resonance image denoising using low-rank tensor approximation, Neurocomputing 195 (2016) 30–39, http://dx.doi.org/10.1016/j.neucom.2015.09.125.

[17] J. Hu, X.W. Jiliu Zhou, Non-local MRI denoising using random sampling, Magn. Reson. Imaging 34 (2016) 990–999, http://dx.doi.org/10.1016/j.mri.2016.04.008.

[18] C. Pal, P. Das, A. Chakrabarti, R. Ghosh, Rician noise removal in magnitude MRI images using efficient anisotropic diffusion filtering, Imaging Syst. Technol. 27 (2017) 248–264, http://dx.doi.org/10.1002/ima.22230.

[19] F. Baselice, G. Ferraioli, V. Pascazio, A. Sorriso, Bayesian MRI denoising in complex domain, Magn. Reson. Imaging 38 (2017) 112–122, http://dx.doi.org/10.1016/j.mri.2016.12.024.

[20] H.M. Golshan, R.P. Hasanzadeh, An optimized LMMSE based method for 3d MRI denoising, IEEE/ACM Trans. Comput. Biol. Bioinformatics 12 (2015) 861–870.

[21] P.V. Sudeep, P. Palanisamy, C. Kesavadas, J. Rajan, Nonlocal linear minimum mean square error methods for denoising MRI, Biomed. Signal Process. Control 20 (2015) 125–134, http://dx.doi.org/10.1016/j.bspc.2015.04.015.

[22] N. Yaghoobi, R.P. Hasanzadeh, De-noising of 3d multiple-coil MR images using modified LMMSE estimator, Magn. Reson. Imaging 52 (2018) 102–117.

[23] F. Baselice, G. Ferraioli, V. Pascazio, A. Sorriso, Denoising of MR images using Kolmogorov–Smirnov distance in a non-local framework, Magn. Reson. Imaging 57 (2019) 176–193.

[24] K. Dabov, A. Foik, K. Egiazarian, Image denoising by sparse 3-d transform-domain collaborative filtering, IEEE Trans. Image Process. 16 (2007) 2080–2095.

[25] M. Maggioni, V. Katkovnik, K. Egiazarian, A. Foi, Nonlocal transform-domain filter for volumetric data denoising and reconstruction, IEEE Trans. Image Process. 22 (2013) 119–133.

[26] A. Rajwade, A. Rangarajan, A. Banerjee, Image denoising using the higher order singular value decomposition, IEEE Trans. Pattern Anal. Mach. Intell. 35 (2013) 849–862.

[27] X. Zhang, Z. Xu, N. Jia, W. Yang, Q. Feng, W. Chen, Y. Feng, Denoising of 3d magnetic resonance images by using higher-order singular value decomposition, Med. Image Anal. 19 (2015) 75–86.

[28] H.S. Khaleel, S.V.M. Sagheer, M. Baburaj, S.N. George, Denoising of Rician corrupted 3d magnetic resonance images using tensor-SVD, Biomed. Signal Process. Control 44 (2018) 82–95.

[29] Z. Kong, L. Han, X. Liu, X. Yang, A new 4-d nonlocal transform-domain filter for 3-d magnetic resonance images denoising, IEEE Trans. Med. Imaging 37 (2018) 941–954.

[30] F. Lam, S.D. Babacan, J.P. Haldar, M.W. Weiner, N. Schuff, Z.-P. Liang, Denoising diffusion-weighted magnitude MR images using rank and edge constraints, Magn. Reson. Med. 71 (2014) 1272–1284.

[31] Y. Xia, Q. Gao, N. Cheng, Y. Lu, D. Zhang, Q. Yec, Denoising 3-d magnitude magnetic resonance images based on weighted nuclear norm minimization, Biomed. Signal Process. Control 34 (2017) 183–194, http://dx.doi.org/10.1016/j.bspc.2017.01.016.

[32] H.V. Bhujle, B.H. Vadavadagi, NLM based magnetic resonance image denoising – a review, Biomed. Signal Process. Control 47 (2019) 252–261.

[33] D.C. Hoaglin, F.M.J.W. Tukey, Understanding Robust and Exploratory Data Analysis, Wiley, 2000.

[34] M.J. Black, A. Rangarajan, On the unification of line processes, outlier rejection, and robust statistics with applications in early vision, Int. J. Comput. Vis. 19 (1996) 57–91, http://dx.doi.org/10.1007/BF00131148.

[35] H. Gudbjartsson, S. Patz, The Rician distribution of noisy MRI data, Magn. Reson. Med. 34 (1995) 910–914, http://dx.doi.org/10.1002/mrm.1910340618.

[36] R. Henkelman, Measurement of signal intensities in the presence of noise in MR images, Med. Phys. 12 (1985) 232–233, http://dx.doi.org/10.1118/1.595711.

[37] S.O. Rice, Mathematical analysis of random noise, Bell Syst. Techn. J. 23 (1944) 282–332, http://dx.doi.org/10.1002/j.1538-7305.1944.tb00874.

[38] S. Aja-Fernández, G.V. Sanchez-Ferrero, Statistical Analysis of Noise in MRI: Modeling, Filtering and Estimation, Springer International Publishing, 2016, http://dx.doi.org/10.1007/978-3-319-39934-8.

[39] A. den Dekker, J. Sijbers, Data distributions in magnetic resonance images: a review, Phys. Med. 30 (2014) 725–741, http://dx.doi.org/10.1016/j.ejmp.2014.05.002.

[40] H. Gudbjartsson, S. Patz, The Rician distribution of noisy MRI data, Magn. Reson. Med. 34 (1995) 910–914, http://dx.doi.org/10.1002/mrm.1910340618.

[41] J. Sijbers, A.J. den Dekker, P. Scheunders, D.V. Dyck, Maximum-likelihood estimation of Rician distribution parameters, IEEE Trans. Med. Imaging 17 (1998) 357–361, http://dx.doi.org/10.1109/42.712125.

[42] P. Coupé, J.V. Manjón, E. Gedamu, D. Arnold, M. Robles, D.L. Collins, Robust Rician noise estimation for MR images, Med. Image Anal. 14 (2010) 483–493, http://dx.doi.org/10.1016/j.media.2010.03.001.

[43] C.G. Koay, P.J. Basser, Analytically exact correction scheme for signal extraction from noisy magnitude MR signals, J. Magn. Reson. 179 (2006) 317–322, http://dx.doi.org/10.1016/j.jmr.2006.01.016.

[44] M. Black, P. Anandan, Robust dynamic motion estimation over time, Comput. Vis. Pattern Recogn. 4132440 (1991) 296–302.

[45] F.R. Hampel, E.M. Ronchetti, P.J. Rousseeuw, W.A. Stahel, Robust Statistics: The Approach Based on Influence Functions, Wiley, 2011.

[46] P.J. Rousseeuw, A.M. Leroy, Robust Regression and Outlier Detection, Wiley Series in Probability and Statistics, 2003, http://dx.doi.org/10.1002/0471725382.

[47] K.K. Talukdar, W.D. Lawing, Estimation of the parameters of the rice distribution, J. Acoust. Soc. Am. 89 (1990) 1193–1197, http://dx.doi.org/10.1121/1.400532.

[48] S. Aja-Fernández, T. Pieciak, G.V. Sanchez-Ferrero, Spatially variant noise estimation in MRI: a homomorphic approach, Med. Image Anal. 20 (2015) 184–197, http://dx.doi.org/10.1016/j.media.2014.11.005.

[49] M. Abramowitz, I.A. Stegun, Handbook of Mathematical Functions, 1964.

[50] J. Sijbers, A.J. den Dekker, E. Raman, D.V. Dyck, Parameter estimation from magnitude MR images, Int. J. Imaging Syst. Technol. 10 (1999) 109–114, http://dx.doi.org/10.1002/(SICI)1098-1098(1999)10:2<109::AID-IMA2>3.0.CO;2-R.

[51] D. Collins, A. Zijdenbos, J.S.V. Kollokian, N. Kabani, C. Holmes, A. Evans, Design and construction of a realistic digital brain phantom, IEEE Trans. Med. Imaging 17 (1998) 463–468, http://dx.doi.org/10.1109/42.712135.

[52] A. Eskicioglu, P. Fisher, Image quality measures and their performance, IEEE Trans. Commun. 43 (1995) 2959–2965, http://dx.doi.org/10.1109/26.477498.

[53] Z. Wang, A.C. Bovik, H.R. Sheikh, E.P. Simoncelli, Image quality assessment: from error visibility to structural similarity, IEEE Trans. Image Process. 13 (2004) 600–612, http://dx.doi.org/10.1109/TIP.2003.819861.

[54] F. Liu, J.V. Velikina, W.F. Block, R. Kijowski, A.A. Samsonov, Fast realistic MRI simulations based on generalized multi-pool exchange tissue model, IEEE Trans. Med. Imaging 36 (2017) 527–537.

[55] A.F. Fotenos, A.Z. Snyder, L.E. Girton, J.C. Morris, R.L. Buckner, Normative estimates of cross-sectional and longitudinal brain volume decline in aging and AD, Neurology 64 (2005).